

## Article

# Effect of Ca and Sb on the Corrosion Resistance of E690 Steel in Marine Atmosphere Environment

Jianbo Jiang<sup>1,2</sup>, Nannan Li<sup>3</sup>, Qinglin Li<sup>3</sup>, Zaihao Jiang<sup>3,\*</sup>, Bingqin Wang<sup>3,\*</sup> , Yinyin He<sup>3</sup>, Fangfang Liu<sup>1,2</sup> and Chao Liu<sup>3</sup>

<sup>1</sup> State Key Laboratory of Metal Material for Marine Equipment and Application, Anshan 114009, China

<sup>2</sup> Ansteel Beijing Research Institute Co., Ltd., Beijing 102209, China

<sup>3</sup> Institute of Advanced Materials & Technology, University of Science and Technology Beijing, Beijing 100083, China

\* Correspondence: jiangzaihaoustb@163.com (Z.J.); d202110692@xs.ustb.edu.cn (B.W.); Tel.: +86-010-5333-3931 (Z.J. & B.W.)

**Abstract:** This study investigates the impact of Ca and Sb elements on the corrosion resistance of E690 steel in a simulated marine environment. Electrochemical testing and dry/wet cyclic corrosion testing were conducted on prepared E690 steel specimens. The eroded specimens' microstructure was observed under a scanning electron microscope, and the inclusion morphology was analyzed using an energy-dispersive spectrometer (EDS). The simulating liquid was designed to emulate the severe marine atmospheric environment in Xisha. Results showed that the addition of Ca and Sb elements effectively enhances the corrosion resistance of E690 steel in the simulated marine environment. The corrosion rates of E690 steel specimens with Ca and Sb additions were lower than those without, and the corrosion morphology was more uniform. These findings suggest that the addition of Ca and Sb elements can improve the corrosion resistance of E690 steel in simulated marine environments and have potential for use in marine engineering applications.

**Keywords:** low alloy steel; alloy adjustment; atmospheric corrosion; corrosion resistance



**Citation:** Jiang, J.; Li, N.; Li, Q.; Jiang, Z.; Wang, B.; He, Y.; Liu, F.; Liu, C. Effect of Ca and Sb on the Corrosion Resistance of E690 Steel in Marine Atmosphere Environment. *Metals* **2023**, *13*, 826. <https://doi.org/10.3390/met13050826>

Academic Editors: Reza Parvizi and Anthony Hughes

Received: 4 April 2023

Revised: 19 April 2023

Accepted: 20 April 2023

Published: 23 April 2023



**Copyright:** © 2023 by the authors. Licensee MDPI, Basel, Switzerland. This article is an open access article distributed under the terms and conditions of the Creative Commons Attribution (CC BY) license (<https://creativecommons.org/licenses/by/4.0/>).

## 1. Introduction

The use of steel in marine environments is essential for various marine engineering applications [1]. However, the harsh atmospheric conditions of the marine environment can cause the corrosion of steel [2–4], which can lead to significant economic losses and safety hazards. As a result [5–7], researchers and industry professionals are highly interested in enhancing the corrosion resistance of steel in marine environments [8].

Several methods have been proposed to improve the corrosion resistance of steel in marine environments [9–11]. These methods include the addition of corrosion inhibitors [12,13], coatings [14–16], and alloying elements [13,17,18]. Corrosion inhibitors, such as organic and inorganic compounds, have been extensively studied and shown to effectively reduce the corrosion rate of steel in seawater [19]. Similarly, coatings, such as paints and epoxy, have been shown to provide a protective barrier against corrosion [20]. Alloying elements, such as chromium and nickel, have been added to steel to enhance its corrosion resistance in seawater [21]. These methods have been shown to be effective in improving the corrosion resistance of steel in the marine environment and are therefore of great interest to the maritime industry. Among them, low alloy steel (LAS) is a type of steel that contains a small number of alloying elements. Due to its composition, LAS offers several advantages over conventional carbon steel, including improved mechanical properties, higher strength, and greater toughness. Additionally, LAS has excellent corrosion resistance [22–24], which makes it an ideal choice for use in harsh environments where traditional carbon steel would quickly corrode. According to a study by Klassert [21], LAS containing elements such as chromium, molybdenum, and nickel exhibit superior corrosion resistance compared to

carbon steel, particularly in acidic environments. Another study by Kearns [25] highlights the importance of controlling the composition of LAS to optimize its corrosion resistance properties. In summary, low alloy steel offers significant advantages over conventional carbon steel, including superior corrosion resistance, making it an excellent choice for a wide range of industrial and commercial applications. The addition of Ca and Sb elements has demonstrated promising results in enhancing the corrosion resistance of steel. Previous studies have revealed that Ca and Sb elements can effectively inhibit the formation of inclusions in steel and reduce the corrosion rate in various environments [11]. Moreover, previous research has shown that Ca and Sb can form protective films on the surface of the steel, which can inhibit the corrosion process. A study by Tavares [26] found that Ca addition to low-carbon steel effectively improved its corrosion resistance in seawater. Yang [27] showed that the addition of Sb to steel led to the formation of a passivation layer, which reduced the corrosion rate in a saline solution. These findings suggest that the alloying of Ca and Sb can be an effective method for improving the corrosion resistance of steel in the marine environment.

E690 steel is a high-strength low-alloy (HSLA) steel that is commonly used in marine applications due to its excellent strength [28], toughness, and corrosion resistance properties [29,30]. E690 steel is often used in the construction of ships and other marine vessels; it can be used for various components of the ship, including the hull, superstructure, and deck. Furthermore, E690 steel is also commonly used in the offshore oil and gas industry for various applications, such as in the construction of drilling platforms, pipelines, and subsea equipment. Its high strength and corrosion resistance make it well-suited for these harsh environments. In addition, the E690 steel is also used in ocean engineering applications, such as the construction of offshore wind turbines and other renewable energy structures. But it is vulnerable to corrosion in harsh atmospheric conditions such as saltwater, high humidity [31], and acidic gases. Chloride ions in saltwater corrode the steel and weaken its structural integrity, while high humidity and acidic gases accelerate the corrosion process by creating a moist environment and forming acid rain. To prevent corrosion, protective coatings, and regular maintenance are necessary. Additionally, adjusting the alloy ratio can improve the steel's corrosion resistance. However, the effect of Ca and Sb elements on the corrosion resistance of E690 steel in simulated marine environments has not been thoroughly investigated.

In order to further explore ways to improve the corrosion resistance of E690 steel, in this study, the effect of Ca and Sb elements on the corrosion resistance of E690 steel in a simulated marine environment was investigated through electrochemical testing and dry/wet cyclic corrosion testing. The microstructure of the eroded specimens was observed under a scanning electron microscope, and the morphology of the inclusions in the specimens was analyzed by EDS. It has been reported that the addition of Ca and Sb elements can effectively improve the corrosion resistance of E690 steel in the simulated marine environment [28,32]. The corrosion rates of E690 steel specimens with Ca and Sb additions were found to be lower than those without additions, and the corrosion morphology was more uniform. Furthermore, Ca and Sb elements were found to effectively inhibit the formation of inclusions in the steel.

## 2. Materials and Methods

### 2.1. Materials and Solution

In this study, two different compositions of E690 steel, labeled #1 and #2, were used for a comparative study. The tested steel was produced using a 10 kg vacuum induction furnace for smelting. The chemical composition of the steel is provided in Table 1. In the hot rolling process, the billet was forged into an L × 60 mm × 30 mm steel plate, which was heated to 1200 °C for 2 h. The furnace was then cooled to 1000 °C to begin rolling, which was done three times. The final rolling temperature was controlled to be near 880 °C, and the final thickness of the steel plate was controlled to be 15 mm. The rolled steel plate was then cooled to 420~440 °C using water and finally air-cooled to room temperature.

**Table 1.** Chemical composition of E690 steel (wt.%).

	C	Si	Mn	P	S	Cr	Cu	Ni	Al	Nb	Ca	Sb	Fe
1#	0.055	0.73	1.53	0.0061	0.0029	0.91	0.44	0.90	0.010	0.093	-	-	Bal.
2#	0.052	0.81	1.60	0.0067	0.0034	0.90	0.42	0.86	0.0025	0.15	0.0004	0.095	Bal.

The solution was used to simulate the marine atmospheric environment in Xisha. The composition of the solution was NaCl 0.1 wt %, Na<sub>2</sub>SO<sub>4</sub> 0.05 wt %, CaCl<sub>2</sub> 0.05 wt %, and pH = 5.0.

### 2.2. Microstructure Observation

For this study, specimens measuring 10 mm × 10 mm × 5 mm were used and polished using 5000 mesh sandpaper. After polishing, the specimens were cleaned using anhydrous ethanol in an ultrasonicator and then dried with a high-pressure air gun. Prior to testing, the specimens were eroded using a 4% nitric acid alcohol solution for 3 s and then rinsed with deionized water and anhydrous ethanol. The microstructure of the eroded specimens was analyzed using field emission scanning electron microscopy (FE-SEM, SU8220, Hitachi, Japan) and energy disperse spectroscopy (EDS) at a working voltage of 10 kV and a working distance of 10 mm.

### 2.3. Electrochemical Testing

To prepare the specimen for electrochemical testing, a 10 mm × 10 mm × 5 mm steel specimen was soldered to a copper wire and then sealed with epoxy resin, exposing only one surface of 10 mm × 10 mm. The exposed surface of the specimen was polished with 2000 mesh silicon carbide sandpaper using a water mill, cleaned with anhydrous ethanol and deionized water, and dried with compressed air. Electrochemical tests were performed using a Versa-STAT3 (Princeton, NJ, USA) electrochemical workstation with a standard three-electrode system. The working electrode was the steel specimen, a Pt sheet was used as the auxiliary electrode, and the saturated calomel electrode (SCE) was used as the reference electrode.

The electrochemical experiments were conducted at room temperature, and the electrochemical impedance spectra (EIS) were measured at the open-circuit potential (OCP) with an excitation potential of 10 mV and a frequency range of 100 kHz to 10 mHz. Each set of experiments was repeated three times. The results were fitted with Z-Simp Win software. The electrochemical polarization curve was scanned forward from −0.3 V (SCE) to 0.8 V (SCE) at a scan rate of 0.1667 mV/s. Prior to starting the electrochemical scan, a stable OCP was obtained. The experimental results were analyzed with EC-lab software.

### 2.4. Dry/Wet Cyclic Corrosion Test

The specimens underwent a simulated corrosion test, wherein they were alternatively immersed in Sisal simulating liquid and dried in air. This test aimed to replicate the corrosive effects of the harsh marine atmosphere's alternating dry and wet environment, which causes the liquid level to rise and fall. The pegged specimens were sized at 50 mm × 25 mm × 3 mm, and each group consisted of three parallel pegs. The pegs were polished with silicon carbide sandpaper to 800 mesh, cleaned with alcohol, and their initial weight, length, width, and height were recorded. The experiment was conducted for 120 h, 240 h, and 360 h, respectively, at an ambient temperature of 35 °C. Each cycle lasted for 1 h, with a soaking time of 15 min and a drying time of 45 min. The pegs underwent rust removal after each weekly soaking experiment. They were first cleaned with acetone, then treated with a rust removal solution consisting of 500 mL HCl, 500 mL H<sub>2</sub>O, and 3–10 g hexamethyl tetramine. The specimens were subjected to ultrasonic cleaning to remove corrosion products, rinsed with deionized water, and dried with acetone. The weight of the

specimen after weight loss was recorded, and the uniform corrosion rate of the specimen was calculated using Equation (1) [16]:

$$CR = 8.76 \times 10^4 \times W/S \times \rho \times t \quad (1)$$

where CR is the corrosion rate (mm/y), W is the weight loss mass (g), S is the surface area of the specimen (cm<sup>2</sup>),  $\rho$  is the density of the specimen (g/cm<sup>3</sup>), and t is the length of the weekly immersion experiment (h).

### 2.5. Rust Layer Characterization Method

After dry/wet cyclic corrosion test. The corrosion morphology of the specimen surface after rust removal and the depth of corrosion pitting were observed using a laser confocal microscope (KEYENCE-X250, Osaka, Japan). To ensure that the sampling points were evenly distributed and that both internal and external rust layers were taken, the specimen was soaked and blown dry, and the corrosion products on the surface were scraped off using mechanical methods. The sample was then placed in a drying dish to prevent dehydration, dried, and ground into a powder with a particle size of less than 10  $\mu$ m to achieve the conditions of no selective orientation and small grain size. The corrosion products were characterized using Jade software and a BRUCKER D8 X-ray diffractometer with a Co target in the range of 10–90° and a scan rate of 4°/min.

The rust layer was sealed with epoxy resin, grounded to 1200 mesh with SiO<sub>2</sub> sandpaper, polished briefly, and cleaned and dried with acetone. The surface was sprayed with gold for observation using a scanning electron microscope (SEM-EDS, JEOL JSM-7100F, Tokyo, Japan) to analyze the cross-sectional morphology and elemental distribution of the rust layer.

## 3. Results

### 3.1. Microstructure Characterization

As shown in Figure 1, specimens 1# and 2# exhibit a typical slatted bainite microstructure where the original austenite grain boundaries are faintly visible. Another important feature of the slatted bainite organization is the presence of fine M/A islands (martensite + austenite residual) particles that are arranged in an orderly manner. The direction of the M/A island arrangement is roughly parallel to the slats and tends to be straight. It is widely acknowledged that the slat bainite organization is more uniform and corrosion-resistant than the traditional ferrite + pearlite organization in weathering steel [33–35].

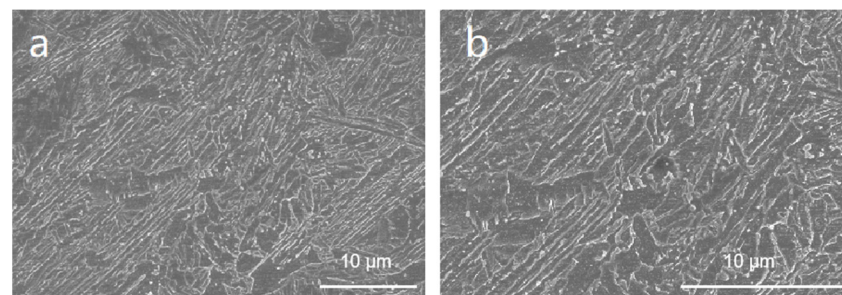


**Figure 1.** The microstructure of the experimental steels, (a) 1# steel, (b) 2# steel.

After conducting the dry/wet cyclic corrosion test and removing the rust from the specimens, the corrosion morphology of the steel substrate surface was examined using a laser confocal microscope. The results presented in Figure 2a,b indicated that after 120 h of testing, the surface of the samples exhibited localized corrosion morphology. The 1# steel sample showed some relatively open corrosion pitting resulting from the fusion of some corrosion pitting, whereas the corrosion pitting of the 2# sample was smaller in both vertical and horizontal dimensions, and the formed corrosion pitting was relatively isolated.

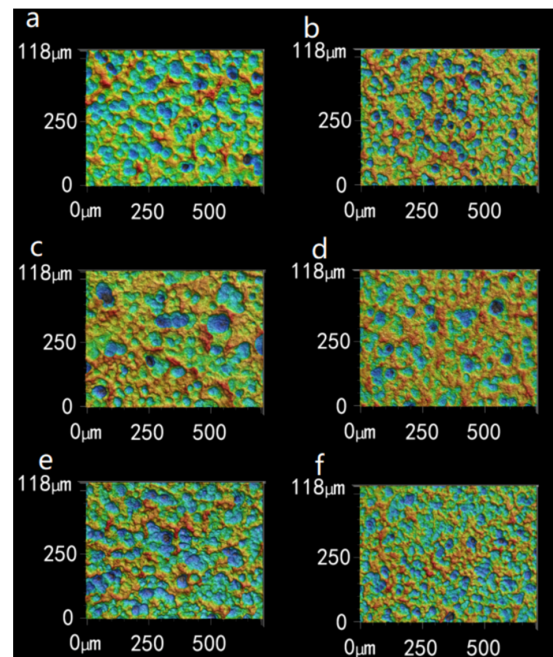


**Figure 2.** The corrosion morphology of samples after dry/wet cyclic corrosion test of different times in the Xisha marine atmosphere simulated solution, (a,c,e) 1# steel, (b,d,f) 2# steel, (a,b) 120 h, (c,d) 240 h, (e,f) 360 h.

After 240-h and 360-h tests, both 1# and 2# samples showed obvious characteristics of uniform corrosion (Figure 2c,d). Based on the images, it was observed that the two steel substrates had been dissolved in a large area, and the width of the corrosion spot on the surface of the sample had significantly expanded since the 120 h immersion test. The depth and width of the corrosion pits of the 1# sample were significantly larger than 2#. Even after the 360 h immersion test (Figure 2e,f), deep and wide corrosion pits were still present on the surface of 1# steel, with some areas showing the corrosion pits merging. Meanwhile, the corrosion morphology of the 2# sample was smoother, with no larger and deeper corrosion pits observed, indicating a high degree of uniform corrosion and good flatness.

The results of statistical mapping of the depth of corrosion pitting on the surface of 1# steel and 2# steel samples are shown in Figure 3. It can be seen from the statistical results that with the increase of time, the depth of corrosion pitting on the surface of 1# and 2# steel has decreased, but the depth of corrosion pits on the surface of 2# steel is smaller than that of 1# steel. Further deepening makes the corrosion uniformity of 2# steel better.

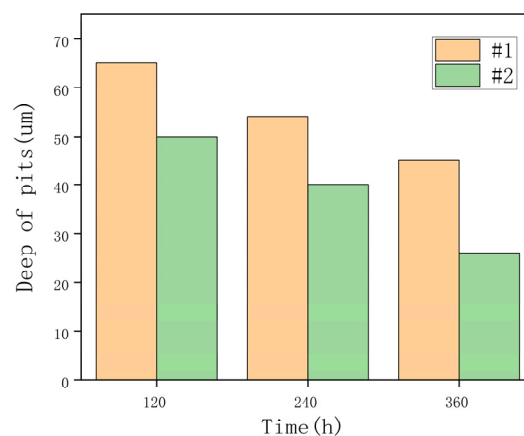


**Figure 3.** Statistical results of pit depth on the sample surface.

### 3.2. Study of Corrosion Kinetics Rules

To investigate the electrochemical behavior of E690 alloy fine-tuned steel at the early stage of corrosion, the polarization curves of 1# and 2# specimens were compared. The specimens were not immersed, immersed for 4 h, and immersed for 12 h in the simulation solution, as shown in Figure 4. It has been reported that at the early stage of corrosion, the polarization curves of the two sheets of steel in the simulation solution exhibited little difference, and both cathodic and anodic processes were controlled by activation. However, the potential of the polarization curve of 1# steel decreased significantly with the extension of the immersion time, whereas the change of the electric polarization curve of 2# with the extension of the immersion time was not significant [28].

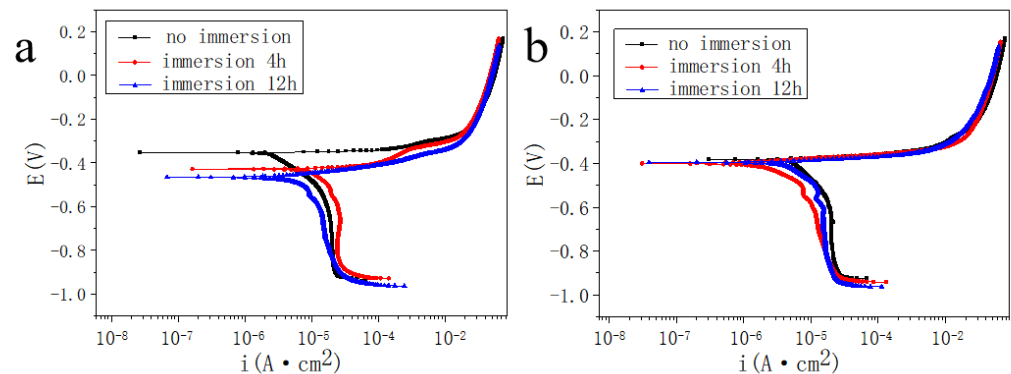


**Figure 4.** The electrochemical polarization curves of the experimental steel after immersion different time, (a) 1# steel, (b) 2# steel.

The  $E_{\text{corr}}$  (corrosion potential) and  $I_{\text{corr}}$  (corrosion current density) of two sheets of steel were obtained after fitting the polarization curve data, and the results are shown in Figure 5. The corrosion potential of 1# steel was slightly higher than that of 2# steel before immersion. However, after immersion for 4 h, the corrosion potential of 2# steel was about 25 mV higher than that of 1# steel, and after 12 h of immersion, it was significantly higher by about 70 mV. The corrosion current density of 2# steel was higher than that of 1# sample without immersion. As the immersion time prolonged, the corrosion current density of 1# continued to rise, although the upward trend gradually slowed down. The corrosion current density of 2# steel first decreased significantly and then increased, but it was generally lower than the corrosion current density when it was without immersion. When the immersion time was longer than 4 h, the corrosion current density of 2# steel was always lower than that of 1# steel. These results suggest that the corrosion activity of 2# steel was slightly higher than that of 1# steel at the initial stage of corrosion, and the corrosion activity was significantly lower than that of 1# steel as the immersion time prolonged. The rust layer on the surface of 2# steel was found to be more protective than that of 1# steel, which increased the resistance of oxygen diffusion and resulted in a decrease in corrosion current density and a slowdown trend of corrosion potential.

Figure 6 shows the electrochemical impedance spectrum and equivalent circuit diagram of the 1# and 2# samples in the Xisha simulated solution. In the diagram,  $R_s$  represents the solution resistance,  $Q_f$  and  $R_f$  represent the constant-phase element of the rust layer and its resistance, respectively, while  $Q_{dl}$  and  $R_{ct}$  represent the double-layer capacitance and charge transfer resistance, respectively. The AC impedance data of the two sheets of steel after different immersion times were analyzed and fitted, and the results are presented in Table 2.

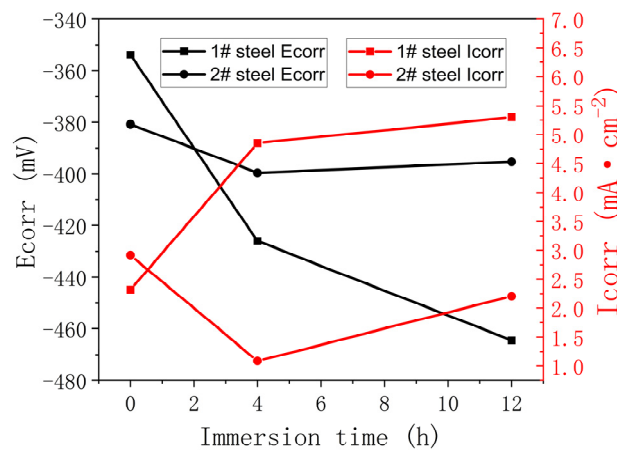


Figure 5. The Ecorr and Icorr of the experimental steel after immersion different time.

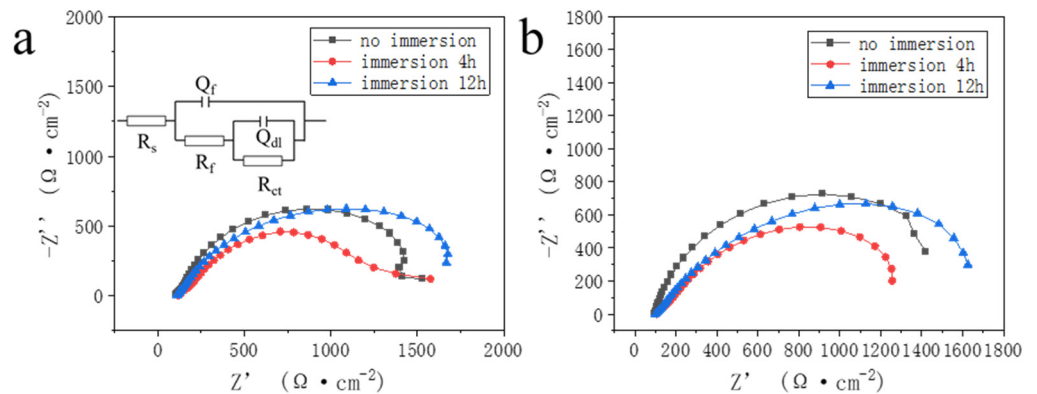
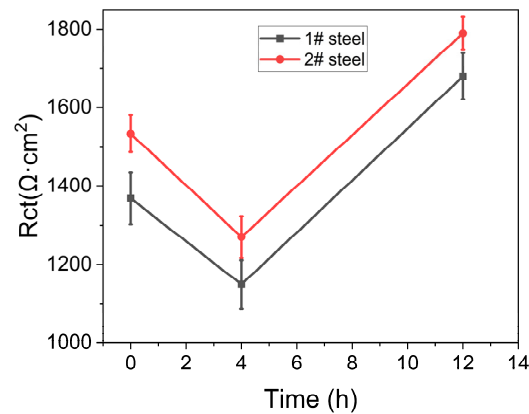


Figure 6. The Nyquist plots with equivalent circuit diagram in of the experimental steels after immersion different time: (a) 1# steel, (b) 2# steel.

Table 2. Fitting parameters of EIS of e690 steel in Xisha marine atmosphere simulated solution.

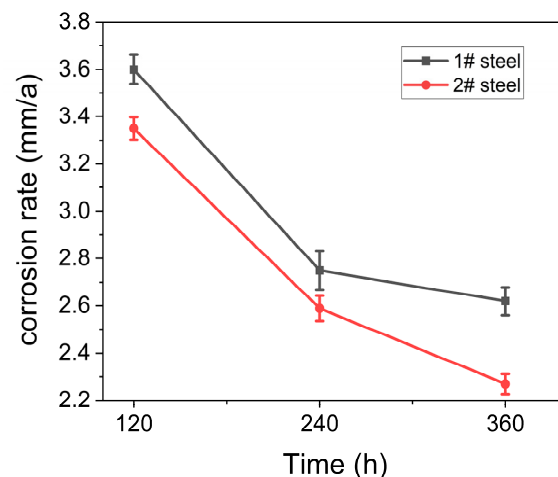
	Time	$R_s$ ( $\Omega \cdot \text{cm}^2$ )	$Q_f$ ( $\mu\text{F}$ $\cdot \text{cm}^{-2} \cdot \text{sn}^{-1}$ )	nf	$R_f$ ( $\Omega \cdot \text{cm}^2$ )	$Q_{dl}$ ( $\mu\text{F}$ $\cdot \text{cm}^{-2} \cdot \text{sn}^{-1}$ )	ndl	$R_{ct}$ ( $\Omega \cdot \text{cm}^2$ )
1#	0 h	105.5	$4.184 \times 10^{-4}$	0.8372	103.5	$4.441 \times 10^{-4}$	0.9133	1369
	4 h	119.5	$6.284 \times 10^{-5}$	0.7763	145.7	$1.204 \times 10^{-3}$	0.8572	1149
	12 h	107.7	$5.820 \times 10^{-4}$	0.7356	155	$2.862 \times 10^{-4}$	0.7758	1680
2#	0 h	96.71	$1.871 \times 10^{-3}$	0.9089	96.52	$7.913 \times 10^{-4}$	0.8816	1534
	4 h	109	$8.698 \times 10^{-4}$	0.7535	134.7	$1.124 \times 10^{-3}$	0.8398	1270
	12 h	100.9	$6.634 \times 10^{-4}$	0.8	104.3	$7.467 \times 10^{-4}$	0.8	1790

Figure 7 shows a comparison diagram of the charge transfer resistance of 1# and 2# sheets of steel in Xisha marine atmosphere simulated solution. It was observed that the charge transfer resistance of both steel samples decreased with an increase in immersion time up to 4 h, and then significantly increased after 12 h. This behavior can be attributed to the fact that as a corrosion reaction occurs, the charge transfer resistance of the corrosion area on the sample surface decreases. Moreover, the charge transfer resistance of 2# steel was found to be higher than that of 1# steel, indicating that alloy adjustment can improve the charge transfer resistance of E690 steel.



**Figure 7.** The charge transfer resistance of two sheets of steel after 0 h, 4 h, and 12 h immersion in Xisha marine atmosphere simulated solution.

The corrosion rates of 1# and 2# sheets of steel were measured after different cycles of dry/wet cyclic corrosion tests, and the results are presented in Figure 8. It was observed that the corrosion rate of both 1# and 2# steel decreased with the extension of the test time. Additionally, the corrosion rate of 2# steel was significantly lower than that of 1# steel. These results suggest that fine-tuning Ca and Sb element alloys can effectively reduce the corrosion rate of E690 steel in the Xisha marine atmosphere simulated solution.



**Figure 8.** The corrosion rates of two sheets of steel after 120 h, 240 h, and 360 h dry/wet cycle corrosion tests.

### 3.3. Study of Rust Layer Morphology

After conducting a 120-h cycle immersion test on the 1# and 2# E690 steel samples, the thickness of the rust layer was measured. The average thickness of the rust layer on 1# steel was  $210 (\pm 7.5) \mu\text{m}$ , and that on 2# steel was  $200 (\pm 4.2) \mu\text{m}$ , indicating little difference between the two (Figure 9). The EDS analysis of the rust layer element distribution map revealed that both samples had an obvious enrichment of the S element in the inner rust layer near the steel substrate, while the enrichment of the Cl element was not significant. The Cr element was found to be significantly enriched in the inner rust layer of both sheets of steel, with a larger and deeper enrichment area and degree in 2# steel. Research has shown that the enrichment of Cr in the inner rust layer can promote the formation of a protective  $\alpha\text{-FeOOH}$  layer and allow Cr atoms to replace the position of Fe in  $\alpha\text{-FeOOH}$  in the inner rust layer form  $\alpha\text{-(Fe}_{1-x}\text{, Cr}_x\text{)OOH}$ , in which fine grains can promote the formation of a dense rust layer [36].

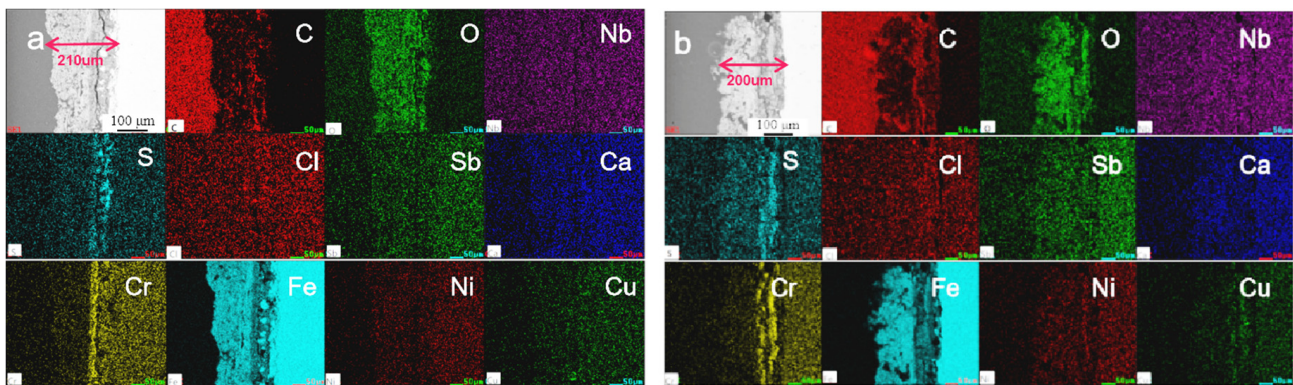


**Figure 9.** Cross-sectional morphology and element distribution of the rust layer formed on the experimental steels after 120 h dry/wet cyclic corrosion test: (a) 1# steel, (b) 2# steel.

Furthermore, the substance also exhibits anion exclusion, which prevents corrosive ions like  $\text{Cl}^-$  and  $\text{SO}_4^{2-}$  from permeating the inner rust layer and reaching the substrate's surface. The Ni element generates stable  $\text{Fe}_2\text{NiO}_4$  in the early stages of corrosion, promotes the formation of a cation-selective rust layer, and effectively reduces the migration of  $\text{Cl}^-$ , and improves the steel's corrosion resistance. The accumulation of S element in the inner rust layer is not found near the steel substrate, indicating that corrosive ions such as  $\text{SO}_4^{2-}$  do not permeate the inner rust layer to reach the substrate's surface. This may be due to the outer rust layer being relatively loose while the inner rust layer is denser and exhibits anion exclusion.

Figure 10 presents the cross-sectional analysis results of the rust layer of two sheets of steels after immersion for 360 h. The average thickness of the rust layer on 1# steel was found to be  $247.5 (\pm 10.2) \mu\text{m}$ , while that on 2# steel was only  $227.3 (\pm 8.4) \mu\text{m}$ , indicating a significant reduction in the thickness of the rust layer in 2# steel. Moreover, the inner rust layer of 2# steel was found to be denser and more uniform compared to that of 1# steel. Interestingly, Figure 8b reveals significant  $\text{Cl}^-$  element enrichment at the interface between the inner rust layer and the outer rust layer of 2# steel, indicating that the rust layer formed on the surface of the steel after alloying regulation can significantly block  $\text{Cl}^-$ .

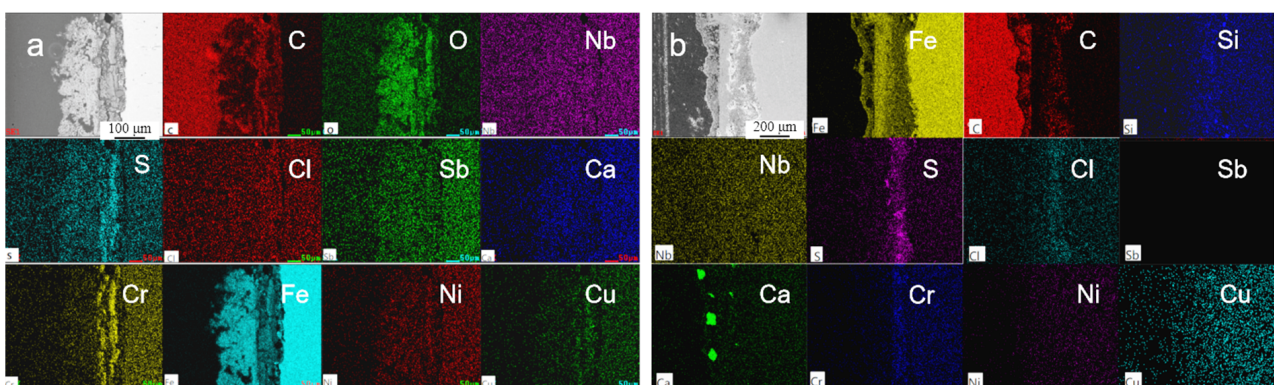


**Figure 10.** Cross-sectional morphology and element distribution of the rust layer formed on the experimental steels after 360 h dry/wet cyclic corrosion test: (a) 1# steel, (b) 2# steel.

### 3.4. Composition of Corrosion Products

The X-ray diffraction (XRD) patterns of the two sheets of steel are shown in Figure 11. Both patterns indicate that  $\text{Fe}_3\text{O}_4$ ,  $\alpha\text{-FeOOH}$ ,  $\gamma\text{-FeOOH}$ ,  $\beta\text{-FeOOH}$ , and  $\text{Fe}_2\text{O}_3$  (Hematite) are the main constituents of the rust layer. Among these,  $\text{Fe}_3\text{O}_4$  is the dominant component, and its dense layer enhances the material's corrosion resistance [37].  $\gamma\text{-FeOOH}$  and  $\beta\text{-FeOOH}$  are considered early corrosion products under alternating dry and wet conditions,

and they can promote corrosion initiation and development [38]. On the other hand,  $\alpha$ -FeOOH is a stable corrosion product formed later, with good continuity and compactness, and is non-conductive, which can protect the steel matrix effectively [39]. The ratio of  $\alpha$ -FeOOH to  $\gamma$ -FeOOH content can be used to assess the protective performance of the rust layer on the steel surface [40]. The semi-quantitative analysis showed that the ratios of  $\alpha$ -FeOOH and  $\gamma$ -FeOOH in the rust layer of 1# and 2# steel were 0.24 and 0.36, respectively, indicating that the protective performance of the rust layer was significantly improved after alloying.

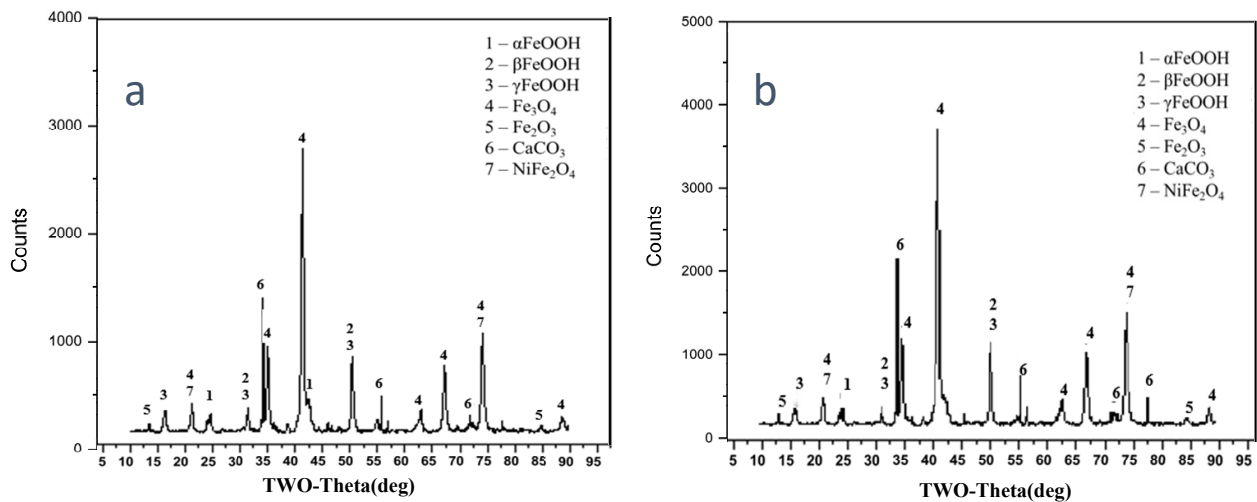


**Figure 11.** Phase compositions of the corrosion products formed on five steels after dry/wet cyclic corrosion test of 360 h, (a) 1# steel, (b) 2# steel.

The XRD results of both steels showed the presence of CaCO<sub>3</sub>, with only 2# steel showing a more obvious presence, consistent with the Ca enrichment phenomenon observed in the outer rust layer of the 2# sample during EDS. The CaCO<sub>3</sub> in 1# steel may have been derived from the adsorption of CaCl<sub>2</sub> and CO<sub>2</sub> in the simulated ocean solution. No Cu and Sb compounds were detected in 2# steel, indicating that the synergistic effect between Cu and Sb elements mentioned in the literature was not successfully observed and that compounds containing the two elements may be related to their low content.

### 3.5. Discussion

The slatted bainite organization of the E690 alloy fine-tuned steel, which consists of fine M/A island particles arranged in an orderly manner, may have contributed to its superior corrosion resistance compared to the traditional ferrite + pearlite organization found in weathering steel [41]. The results also suggest that the corrosion activity of 2# steel is initially slightly higher than that of 1# steel but becomes significantly lower with prolonged immersion time. This is likely due to the more protective rust layer on the surface of 2# steel, resulting in a decrease in corrosion current density and a slowdown in the trend of corrosion potential. Further research is needed to understand the mechanism behind the formation of the protective rust layer on 2# steel and its long-term effect on its corrosion behavior [42]. Additionally, exploring the potential applications of slatted bainite organization and fine M/A island particles may lead to the development of new corrosion-resistant materials.

The charge transfer resistance of 1# and 2# steels in the Xisha marine atmospheric simulation fluid was studied. Interestingly, the charge transfer resistance of both sheets of steel decreased after 4 h of immersion but increased significantly after 12 h, possibly due to the accumulation of corrosion products on the surface of the steel, which hindered the diffusion of oxygen and other species, resulting in an increase in the charge transfer resistance [43]. Additionally, the charge transfer resistance of 2# steel was higher than that

of 1# steel, indicating that the alloy adjustment made to the E690 steel effectively improved its charge transfer resistance [32,44]. This suggests that the slatted bainite organization and fine M/A island particles might have contributed to the improvement in the charge transfer resistance of 2# steel compared to 1# steel.

The addition of Ca and Sb elements to E690 steel can reduce its corrosion rate in the Xisha marine environment [45]. Enrichment of Cr in the inner rust layer promotes the formation of a dense rust layer and cation selectivity, preventing the passage of corrosive ions. Uniform distribution of Nb and Ni elements in the steel and rust layers promotes a positive change in the self-corrosion potential and increased rust layer density [46,47]. The main components of the rust layer on both sheets of steel are  $\text{Fe}_3\text{O}_4$ ,  $\alpha\text{-FeOOH}$ ,  $\gamma\text{-FeOOH}$ ,  $\beta\text{-FeOOH}$ , and  $\text{Fe}_2\text{O}_3$ . The ratio of  $\alpha\text{-FeOOH}$  to  $\gamma\text{-FeOOH}$  can reflect the rust layer's protective performance, and the semi-quantitative results indicate a significant improvement in the protective performance after alloying [48]. Only 1# steel showed the presence of  $\text{CaCO}_3$  in the XRD results.

#### 4. Conclusions

This study investigated the influence of Ca and Sb elements on the corrosion resistance of E690 steel in a simulated Xisha marine environment, and the following conclusions were drawn:

(1) The macroscopic electrochemical experiments showed that with the increase in immersion time, the corrosion potential of 2# steel fine-tuned by Ca and Sb element alloys was increasingly higher than that of 1# steel with the same immersion time. Additionally, the charge transfer resistance of 2# steel was significantly higher than that of 1# steel at different test times, suggesting that alloy fine-tuning could improve the charge transfer resistance and corrosion potential of E690 steel, thereby enhancing the electrochemical stability and corrosion resistance of the steel.

(2) In the periodic immersion test, the corrosion rates of 1# steel and 2# steel gradually decreased with the prolongation of the dry/wet cyclic corrosion test time, and the corrosion rate of 2# steel was lower than that of 1# steel at different time points. This suggests that the fine adjustment of the Ca and Sb element alloy can reduce the corrosion rate of E690 steel in severe marine environments.

(3) The addition of Ca and Sb elements can significantly improve the compactness and corrosion uniformity of the rust layer on the steel surface, and the depth of corrosion pits on the surface of E690 steel is significantly reduced after alloy adjustment. This indicates that the addition of alloying elements inhibits the longitudinal growth of corrosion pits and improves the corrosion uniformity of the material.

(4) Based on the conclusions of the study, there are several possible avenues for future research. Firstly, further investigation into the effects of other alloying elements on the corrosion resistance of E690 steel in marine environments could lead to the development of even more effective alloys with superior corrosion resistance. Additionally, field testing of E690 steel with Ca and Sb element alloys in actual marine environments would provide valuable insights into the real-world effectiveness of these alloys. Furthermore, studies on the long-term durability of E690 steel with Ca and Sb element alloys could help determine the material's lifespan and maintenance requirements in marine environments. By exploring these research areas, it is possible to further improve the corrosion resistance and longevity of E690 steel, making it a more reliable and sustainable choice for marine applications.

**Author Contributions:** Methodology, J.J., B.W. and Z.J.; Software, B.W.; Validation, N.L.; Formal analysis, Q.L. and J.J.; Investigation, C.L.; Resources, C.L.; Data curation, J.J. and F.L.; Writing—original draft, J.J.; Writing—review and editing, F.L. and Y.H.; Project administration, Q.L. and Z.J. Funding acquisition, C.L. and J.J. All authors have read and agreed to the published version of the manuscript.

**Funding:** This research was funded by the National Natural Science Foundation of China (No. 52104319).

**Data Availability Statement:** The raw/processed data required to reproduce these findings cannot be shared at this time as the data are related to an ongoing study.

**Conflicts of Interest:** The authors declare no conflict of interest.

## References

1. Zhang, Q.; Jian, W.; Chen, J. The Study on the Corrosion Resistance of Rust Layer on the Surface of Weathering Steel in Marine Atmosphere. *Chin. J. Mater. Sci. Eng.* **2001**, *19*, 12–25. [[CrossRef](#)]
2. Messinese, E.; Casanova, L.; Paterlini, L.; Capelli, F.; Bolzoni, F.; Ormellesse, M.; Brenna, A. A Comprehensive Investigation on the Effects of Surface Finishing on the Resistance of Stainless Steel to Localized Corrosion. *Metals* **2022**, *12*, 1751. [[CrossRef](#)]
3. Khan, M.S.; Liang, T.; Liu, Y.; Shi, Y.; Zhang, H.; Li, H.; Guo, S.; Pan, H.; Yang, K.; Zhao, Y. Microbiologically Influenced Corrosion Mechanism of Ferrous Alloys in Marine Environment. *Metals* **2022**, *12*, 1458. [[CrossRef](#)]
4. Zhao, L.; He, W.; Wang, Y.; Li, H.; Cui, Z. A Comparative Study of the Corrosion Behavior of 30CrMnSiNi2A in Artificial Seawater and Salt Spray Environments. *Metals* **2022**, *12*, 1443. [[CrossRef](#)]
5. Zhou, R.; Chen, W.; Li, W.; Chou, T.-H.; Chen, Y.-H.; Liang, X.; Luan, J.; Zhu, Y.; Huang, J.C.; Liu, Y. 3D printed N-doped CoCrFeNi high entropy alloy with more than doubled corrosion resistance in dilute sulphuric acid. *Npj Mater. Degrad.* **2023**, *7*, 8. [[CrossRef](#)]
6. Daneshian, B.; Höche, D.; Knudsen, O.; Skilbred, A.W.B. Effect of climatic parameters on marine atmospheric corrosion: Correlation analysis of on-site sensors data. *Npj Mater. Degrad.* **2023**, *7*, 10. [[CrossRef](#)]
7. Xu, Y.; Huang, Y.; Cai, F. Study on corrosion, hydrogen permeation, and stress corrosion cracking behaviours of AISI 4135 steel in the tidal zone. *Npj Mater. Degrad.* **2022**, *6*, 96. [[CrossRef](#)]
8. Pandian, B.; Mohammad, I.; Seyedmojtaba, G.; Jahangir, M.; Mokhtar, I.; Kakooei, S. Reviews on corrosion inhibitors: A short view. *Chem. Eng. Commun.* **2016**, *203*, 1145–1156.
9. Liu, W.; Yin, H.; Du, K.; Yang, B.; Wang, D. Corrosion Behaviors of Iron, Chromium, Nickel, Low-Carbon Steel, and Four Types of Stainless Steels in Liquid Antimony-Tin Alloy. *Corrosion* **2021**, *77*, 1192–1202. [[CrossRef](#)]
10. Zheng, C.; Liu, Z.; Chen, S.; Liu, C. Corrosion behavior of a Ni–Cr–Mo alloy coating fabricated by laser cladding in a simulated sulfuric acid dew point corrosion environment. *Coatings* **2020**, *10*, 849. [[CrossRef](#)]
11. Zhang, T.; Li, Y.; Li, X.; Liu, C.; Yang, S.; Yang, Z.; Li, X. Integral effects of Ca and Sb on the corrosion resistance for the high strength low alloy steel in the tropical marine environment. *Corros. Sci.* **2022**, *208*, 110708. [[CrossRef](#)]
12. Abdel-Karim, A.M.; El-Shamy, A.M. A review on green corrosion inhibitors for protection of archeological metal artifacts. *J. Bio-Tribo-Corros.* **2022**, *8*, 35. [[CrossRef](#)]
13. Chen, L.; Lu, D.; Zhang, Y. Organic compounds as corrosion inhibitors for carbon steel in HCl solution: A comprehensive review. *Materials* **2022**, *15*, 2023. [[CrossRef](#)] [[PubMed](#)]
14. Farooq, S.A.; Raina, A.; Mohan, S.; Arvind Singh, R.; Jayalakshmi, S.; Irfan Ul Haq, M. Nanostructured coatings: Review on processing techniques, corrosion behaviour and tribological performance. *Nanomaterials* **2022**, *12*, 1323. [[CrossRef](#)] [[PubMed](#)]
15. Nazari, M.H.; Zhang, Y.; Mahmoodi, A.; Xu, G.; Yu, J.; Wu, J.; Shi, X. Nanocomposite organic coatings for corrosion protection of metals: A review of recent advances. *Prog. Org. Coat.* **2022**, *162*, 106573. [[CrossRef](#)]
16. Xu, C.; Liu, W. Organic-inorganic hybrid corrosion protection coating materials for offshore wind power devices: A mini-review and perspective. *Mol. Cryst. Liq. Cryst.* **2020**, *710*, 74–89. [[CrossRef](#)]
17. Ma, Y.; Yang, Y.; Jia, X.; Zhao, H.; Qu, Z.; Wang, D.; Wang, B. Effect of Welding Heat Input on Microstructure and Properties of Coarse-Grained HAZ of 500 MPa High-Strength Low-Alloy Steel. *Trans. Indian Inst. Metals* **2022**, *75*, 1877–1884. [[CrossRef](#)]
18. Wang, X.; Yang, Z.; Du, L. Research on the Microstructure and Properties of a Flux-Cored Wire Gas-Shielded Welded Joint of A710 Low-Alloy High-Strength Steel. *Crystals* **2023**, *13*, 484. [[CrossRef](#)]
19. Pareek, S.; Jain, D.; Behera, D.; Sharma, S.; Shrivastava, R. A review on inhibitors alleviating copper corrosion in hostile simulated sea-water (3.5 wt.% NaCl solution). *Mater. Today Proc.* **2021**, *43*, 3303–3308. [[CrossRef](#)]
20. Zhang, M.; Xu, H.; Zeze, A.; Liu, X.; Tao, M. Coating performance, durability and anti-corrosion mechanism of organic modified geopolymer composite for marine concrete protection. *Cem. Concr. Compos.* **2022**, *129*, 104495. [[CrossRef](#)]
21. Klassert, A.; Tikana, L. Copper and Copper-Nickel Alloys—An Overview. In *Corrosion Behaviour and Protection of Copper and Aluminium Alloys in Seawater*; Woodhead Publishing: Sawston, UK, 2007; pp. 47–61.
22. Guo, J.; Yang, S.; Shang, C.; Wang, Y.; He, X. Influence of carbon content and microstructure on corrosion behaviour of low alloy steels in a Cl<sup>-</sup> containing environment. *Corros. Sci.* **2009**, *51*, 242–251. [[CrossRef](#)]
23. Chen, Y.Y.; Tzeng, H.J.; Wei, L.I.; Wang, L.; Oung, J.C.; Shih, H.C. Corrosion resistance and mechanical properties of low-alloy steels under atmospheric conditions. *Corros. Sci.* **2005**, *47*, 1001–1021. [[CrossRef](#)]
24. Cetin, D.; Aksu, M.L. Corrosion behavior of low-alloy steel in the presence of *Desulfotomaculum* sp. *Corros. Sci.* **2009**, *51*, 1584–1588. [[CrossRef](#)]
25. Kearns, J.R.; Deverell, H.E. The use of nitrogen to improve the corrosion resistance of FeCrNiMo alloys for the chemical process industries. *Mater. Perform.* **1987**, *26*, 6.

26. Tavares, L.M.; da Costa, E.M.; de Oliveira Andrade, J.J.; Hubler, R.; Huet, B. Effect of calcium carbonate on low carbon steel corrosion behavior in saline CO<sub>2</sub> high pressure environments. *Appl. Surf. Sci.* **2015**, *359*, 143–152. [[CrossRef](#)]
27. Yang, Y.; Cheng, X.; Zhao, J.; Fan, Y.; Li, X. A study of rust layer of low alloy structural steel containing 0.1% Sb in atmospheric environment of the Yellow Sea in China. *Corros. Sci.* **2021**, *188*, 109549. [[CrossRef](#)]
28. Wu, W.; Hao, W.K.; Liu, Z.Y.; Li, X.; Du, C.W.; Liao, W.J. Corrosion behavior of E690 high-strength steel in alternating wet-dry marine environment with different pH values. *J. Mater. Eng. Perform.* **2015**, *24*, 4636–4646. [[CrossRef](#)]
29. Fan, E.; Zhao, Q.; Wang, S.; Liu, B.; Yang, Y.; Huang, Y.; Luo, H.; Li, X. Investigation of the hydrogen-induced cracking of E690 steel welded joint in simulated seawater. *Mater. Sci. Eng. A* **2022**, *854*, 143802. [[CrossRef](#)]
30. Li, Y.; You, Y.; Lv, X. Comparative study on the crack growth behaviours of E690 steel and heat-affected zone microstructures under cathodic potential in artificial seawater based on mechano-electrochemical effect at crack tip. *Corros. Sci.* **2022**, *198*, 110103. [[CrossRef](#)]
31. Cai, J.; Sun, L.; Ma, H.; Li, X. Corrosion characteristics of Q690qE high-strength bridge steel in simulated coastal–industrial environment and its influence on mechanical and corrosion fatigue behaviors. *Constr. Build. Mater.* **2022**, *341*, 127830. [[CrossRef](#)]
32. Li, Q.; Xia, X.; Pei, Z. Long-term corrosion monitoring of carbon steels and environmental correlation analysis via the random forest method. *Npj Mater. Degrad.* **2022**, *6*, 24. [[CrossRef](#)]
33. Jia, J.; Cheng, X.; Yang, X.; Li, X.; Li, W. A study for corrosion behavior of a new-type weathering steel used in harsh marine environment. *Constr. Build. Mater.* **2020**, *259*, 119760. [[CrossRef](#)]
34. Xiao, X.M.; Peng, Y.; Ma, C.Y.; Tian, Z.L. Effects of alloy element and microstructure on corrosion resistant property of deposited metals of weathering steel. *J. Iron Steel Res. Int.* **2016**, *23*, 171–177. [[CrossRef](#)]
35. Liu, Q.; Ma, Q.X.; Chen, G.Q.; Cao, X.; Zhang, S.; Pan, J.L.; Shi, Q.Y. Enhanced corrosion resistance of AZ91 magnesium alloy through refinement and homogenization of surface microstructure by friction stir processing. *Corros. Sci.* **2018**, *138*, 284–296. [[CrossRef](#)]
36. Gong, L.; Xing, Q.; Wang, H. Corrosion behaviors of weathering steel 09CuPCrNi welded joints in simulated marine atmospheric environment. *Anti-Corros. Methods Mater.* **2016**, *63*, 295–300. [[CrossRef](#)]
37. Wu, W.; Cheng, X.; Zhao, J.; Li, X. Benefit of the corrosion product film formed on a new weathering steel containing 3% nickel under marine atmosphere in Maldives. *Corros. Sci.* **2020**, *165*, 108416. [[CrossRef](#)]
38. Li, Q.X.; Wang, Z.Y.; Han, W.; Han, E.H. Characterization of the rust formed on weathering steel exposed to Qinghai salt lake atmosphere. *Corros. Sci.* **2008**, *50*, 365–371. [[CrossRef](#)]
39. Kamimura, T.; Hara, S.; Miyuki, H.; Yamashita, M.; Uchida, H. Composition and protective ability of rust layer formed on weathering steel exposed to various environments. *Corros. Sci.* **2006**, *48*, 2799–2812. [[CrossRef](#)]
40. Ma, H.C.; Liu, Z.Y.; Du, C.W.; Wang, H.R.; Li, X.G.; Zhang, D.W.; Cui, Z.Y. Stress corrosion cracking of E690 steel as a welded joint in a simulated marine atmosphere containing sulphur dioxide. *Corros. Sci.* **2015**, *100*, 627–641. [[CrossRef](#)]
41. Liu, C.; Yuan, H.; Li, X.; Che, Z.; Yang, S.; Du, C. Initiation mechanism of localized corrosion induced by Al<sub>2</sub>O<sub>3</sub>-MnS composite inclusion in low-alloy structural steel. *Metals* **2022**, *12*, 587. [[CrossRef](#)]
42. Zhang, X.; Wei, W.; Cheng, L.; Liu, J.; Wu, K.; Liu, M. Effects of niobium and rare earth elements on microstructure and initial marine corrosion behavior of low-alloy steels. *Appl. Surf. Sci.* **2019**, *475*, 83–93. [[CrossRef](#)]
43. Liu, Y.H.; Cheng, W.L.; Zhang, Y.; Niu, X.; Wang, H.X.; Wang, L.F. Microstructure, tensile properties, and corrosion resistance of extruded Mg-1Bi-1Zn alloy: The influence of minor Ca addition. *J. Alloys Compd.* **2020**, *815*, 152414. [[CrossRef](#)]
44. Xue, W.; Li, Z.; Xiao, K.; Yu, W.; Song, J.; Chen, J.; Dong, C.; Li, X. Initial microzonal corrosion mechanism of inclusions associated with the precipitated (Ti, Nb) N phase of Sb-containing weathering steel. *Corros. Sci.* **2020**, *163*, 108232. [[CrossRef](#)]
45. Guo, L.; Huang, Q.; Zhang, C.; Wang, J.; Shen, G.; Ban, C.; Guo, L. Study on the formation of Mn-P coatings with significant corrosion resistance on Q235 carbon steels by adjusting the ratio of phosphorus to manganese. *Corros. Sci.* **2021**, *178*, 108960. [[CrossRef](#)]
46. Li, B.; Yin, X.; Xue, S.; Li, B.; Mu, P.; Li, J. Facile fabrication of graphene oxide and MOF-based superhydrophobic dual-layer coatings for enhanced corrosion protection on magnesium alloy. *Appl. Surf. Sci.* **2022**, *580*, 152305. [[CrossRef](#)]
47. Wang, Z.; Liu, J.; Wu, L.; Han, R.; Sun, Y. Study of the corrosion behavior of weathering steels in atmospheric environments. *Corros. Sci.* **2013**, *67*, 1–10. [[CrossRef](#)]
48. Jiang, S.; Cao, J.P.; Liu, Z.Y.; Xu, X.X.; Yang, J.W.; Li, X.T. Effect of Ni on the oxidation behavior of corrosion products that form on low alloy steel exposed to a thin electrolyte layer environment. *Corros. Sci.* **2022**, *206*, 110471. [[CrossRef](#)]

**Disclaimer/Publisher’s Note:** The statements, opinions and data contained in all publications are solely those of the individual author(s) and contributor(s) and not of MDPI and/or the editor(s). MDPI and/or the editor(s) disclaim responsibility for any injury to people or property resulting from any ideas, methods, instructions or products referred to in the content.